JOURNAL OF THERMOPHYSICS AND HEAT TRANSFER
Vol. 20, No. 3, July–September 2006

Thermal Shielding of a Reentry Vehicle by Ultra-High-Temperature Ceramic Materials

Rodolfo Monti,* Mario De Stefano Fumo,† and Raffaele Savino‡
University of Naples "Federico II," 80125 Naples, Italy

Reentry vehicles with enhanced aerodynamic performances and high maneuverability require sharp leading edges for the wings and control surfaces and a sharp tip of the fuselage nose where high localized heat fluxes occur. Ultra-high-temperature ceramics, for example, zirconium, hafnium, or titanium diborides, are candidate materials for the sharp edges of reentry vehicles that make use of new thermal protection systems, positioning massive thermal protection systems only at the leading edge of the wings (or at the fuselage tip). The boundary-layer thermal protection concept is illustrated, and the requirements for the geometry and materials of the fuselage nose are identified. It is shown how a sharp nose will protect the fuselage, acting as a lightning rod for the rest of the structure when the vehicle flies at relatively low angles of attack. Systematic numerical analyses are shown for the sphere–cone nose vehicle to compute temperature distributions along the surface and inside the nose structure at different angles of attack. The effects of the chemistry and of the surface catalysis are discussed.

Nomenclature

C_D	=	drag-force coefficient
C_L	=	lift-force coefficient
c_i	=	concentration of ith species
c_p	=	specific heat, J/kg · K
D_i	=	diffusion coefficient of ith species, m^2/s
E	=	kinetic energy, J
$\dot{e}$	=	kinetic energy conversion rate per unit mass
h_i	=	specific enthalpy of ith species, J/kg
M	=	Mach number
m	=	mass, kg
m/S	=	wing loading factor, kg/m^2
Pe	=	Peclet number
$\dot{Q}$	=	thermal load, W
$\dot{q}$	=	surface heat flux, W/m^2
R	=	curvature radius, m
S	=	reference area, m^2
T	=	temperature, K
T_r	=	recovery temperature, K
t	=	time, s
V	=	velocity, m/s
Z	=	altitude, km
α	=	angle of attack
δ_T	=	thermal boundary-layer thickness
ε	=	emissivity
λ	=	thermal conductivity, W/m · K
ρ	=	density, kg/m^3
σ	=	Stephan–Boltzmann constant, W/m^2 · K^4
φ	=	swept angle

Subscripts

c	=	convective
eq	=	chemical equilibrium condition
s	=	solid
sp	=	stagnation point
w	=	wall
wr	=	local radiative equilibrium wall

I. Introduction

THE development of future low-risk reentry vehicles[1] is strongly linked to the capability of employing sharp leading-edge and supersoniclike aerodynamic configurations. This choice is driven by the need to improve safety and allow typical aircraft manoeuvrability. Furthermore, these vehicles show extensive down and cross ranges so that they could return from nearly any point along the orbit and land at different sites (contrary to the space shuttle, which has a very narrow window to land at a preselected site).

The main implications and consequences deriving from the idea of a reentry vehicle that gently decelerates and that gradually converts its enormous kinetic plus potential energy into thermal energy are 1) a long-duration flight at very high altitudes, 2) the need to control the vehicle along the entire flight path, 3) a low wing loading m/S and a high aerodynamic efficiency necessary to follow a low-risk trajectory, and 4) crew protection from the temperature increase (due to the long duration in a hot-skin environment). Each of these implications dictate a number of mission requirements related to an efficient navigation and control system along the entire flight path for a very light thermal protection system based on sharp and thin aerodynamic shapes and an adequate thermal insulation of the crew cabin.

The main requirements can be fulfilled basically by an innovative way of protecting the vehicle structure from the high heat flux occurring along an extended portion of the flight path: the boundary layer thermal protection system[2] (BLTPS) that makes use of the new ultra-high-temperature ceramics[3] (UHTC) positioned in the foreparts of the vehicle. During hypersonic flight, significantly higher heating occurs on a sharp leading edge compared to that on a blunt one; this is due to the well-known functional dependence of the stagnation point heat flux on the inverse of the square root of the nose radius of curvature. Therefore, to use a sharp configuration, new materials capable of withstanding the high temperature achieved at the vehicle leading edges must be developed.

UHTC, for example, titanium, zirconium, hafnium diboride, eventually modified with suitable concentrations of silicon carbide (SiC), are a family of ceramic materials with very high melting

Presented as Paper 2005-3265 at the AIAA/CIRA 13th International Space Planes and Hypersonics Systems and Technologies Conference, Capua, Italy, 16–20 May 2005; received 7 June 2005; revision received 26 August 2005; accepted for publication 26 August 2005.

*Full Professor, Department of Space Science and Engineering, "L.G. Napolitano," P.le V. Tecchio 80. Senior Member AIAA.

†Ph.D. Student, Department of Space Science and Engineering, "L.G. Napolitano," P.le V. Tecchio 80. Member AIAA.

‡Associate Professor, Department of Space Science and Engineering, "L.G. Napolitano," P.le V. Tecchio 80.

temperature and good oxidation resistance in reentry environment.[4] Ground-based arcjet testing demonstrated the potential of these materials in reusable application at temperatures of the order of 2500 K (Ref. 5).

In this paper we present parametric numerical simulations to clarify the importance of some material properties in the design of slender reentry vehicles with particular focus on UHTC material properties. We consider the two most important and qualifying aspects for the implementation of the low-risk trajectory: the BLTPS and the use of UHTC.

II. Identification of Thermal Shielding Requirements

The most relevant characteristic of the low-risk trajectory is that an almost flat time profile of the stagnation point heat flux $\dot{q}_{sp}$ is enforced so that the kinetic and potential energy of the vehicle reentering from low-Earth-orbit (LEO) missions is gradually converted into thermal energy, avoiding the characteristic high peak heat fluxes occurring during blunt-body reentry. Figure 1 shows the basic differences in time profiles between the reentry parameters of a shuttlelike vehicle[6] and of a low-risk vehicle.[1]

To appreciate the difference in the aerothermal behavior of the proposed trajectory with respect to the traditional blunt body (capsule or shuttlelike) trajectories let us plot the kinetic energy conversion rate per unit mass, $\dot{e}$, during the deceleration phase,

$$\dot{e} = \frac{1}{M}\frac{\mathrm{d}E}{\mathrm{d}t} = \frac{\mathrm{d}}{\mathrm{d}t}\left(\frac{V^2}{2}\right) = V\frac{\mathrm{d}V}{\mathrm{d}t} \tag{1}$$

For the two different reentry trajectories, starting from the reentry interface, that is, $t=0$, $Z_0=120$ km, and $V=V_0$, to landing (at $t=t_f$ and $V_f \approx 0$) the time integral of $\dot{e}$, represented by the area beneath the two curves, is

$$\int_0^{t_f} \dot{e}\,\mathrm{d}t \cong \frac{V_0^2}{2} \tag{2}$$

and is equal for both the trajectories cases (Fig. 2).

Figure 2 shows that because the shuttle reentry is characterized by a strong deceleration in a short time, the implication is a value of kinetic energy dissipation rate into thermal energy of the body (and of the surrounding air) higher than in a low-risk trajectory. The thermal load, that is, the time integral of the convective heat flux at the body surface, is a fraction of the total converted energy and strongly depends on the body shape and on the surface point location. The fact that the heat flux will be kept almost constant and that the maximum value of $\sqrt{\rho}V^3$ is smaller for the low-risk trajectory allows the use of sharp-edge bodies with a small radius of curvature at the nose or at the wing tips. The ratio between

$$\dot{Q}_c = \int_S \dot{q}_c(t)\,\mathrm{d}S \tag{3}$$

and

$$MV\frac{\mathrm{d}V}{\mathrm{d}t} = \frac{1}{2}C_D\rho V^3 S \tag{4}$$

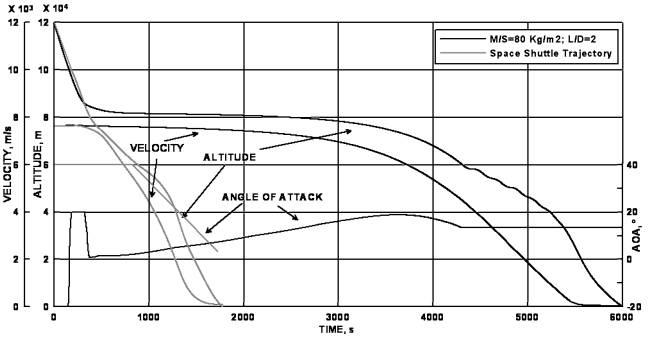

Fig. 1 Low-risk (black) and space shuttle (gray) trajectories.

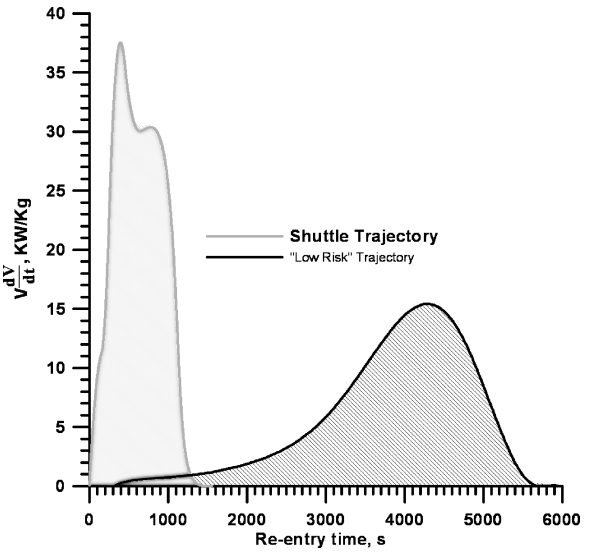

Fig. 2 Kinetic energy conversion rate per unit mass.

represents the fraction of the entire kinetic energy converted into thermal energy convectively entering the body: One would like, therefore, to keep this fraction as small as possible. This ratio depends on the vehicle shape and trajectory. If radiation is being considered, the use of the UHTC materials that can withstand high temperatures allows that a radiative thermal equilibrium to be achieved so that all of the heat that is convectively transferred from the air to the body surface could be radiated back into space. The new way of thermally protecting the vehicle's structural material is made possible by the surface distributions of the convective heat flux that very strongly decreases downstream from the sharp leading edge.

Let us assume that an axisymmetric cone–sphere capsule vehicle flies at hypersonic speed during reentry at zero angle of attack, and let us compute the heat flux over the body surface corresponding to a nose tip of a certain radius of curvature R. In vehicle design, the behavior of the temperature at leading edges is of particular interest because at the stagnation point the boundary layer is very thin and the leading-edge curvature governs the wave drag and the maximum heat flux. Rearranging the Tauber formula[7] and considering the local radiative equilibrium hypothesis for a spherical or cylindrical nose, we have

$$\dot{q}_{sp} = \sigma\varepsilon T_{sp}^4 = \left[K(T_r - T_{sp})\Big/\sqrt{2^n R}\right]\cos\varphi \tag{5}$$

where T_{sp} is the stagnation point temperature, K is a constant depending on the gas, n is 0 for a spherical nose and 1 for a cylindrical nose, φ is the swept angle (zero for a spherical nose and for an unswept wing), and ε is the surface emissivity. If $T_{sp} \ll T_r$, one finds the following general trends.

Spherical nose:

$$T_{sp}^4 \propto 1\Big/\sqrt{R} \tag{6a}$$

Cylindrical leading edge:

$$T_{sp}^4 \propto 1\Big/\sqrt{2R} \tag{6b}$$

Swept cylinder:

$$T_{sp}^4 \propto \cos\varphi\Big/\sqrt{2R} \tag{6c}$$

In this way it is possible to evaluate the leading-edge temperature and, therefore, to design the nose or wings leading-edge radius of the vehicle on the basis of the maximum temperature allowable by the TPS material.

A simple thermal boundary-layer analysis for a radiation cooled wall in hypersonic flow, based on the local equilibrium between convective and radiative heat fluxes, shows that for a flat plate at

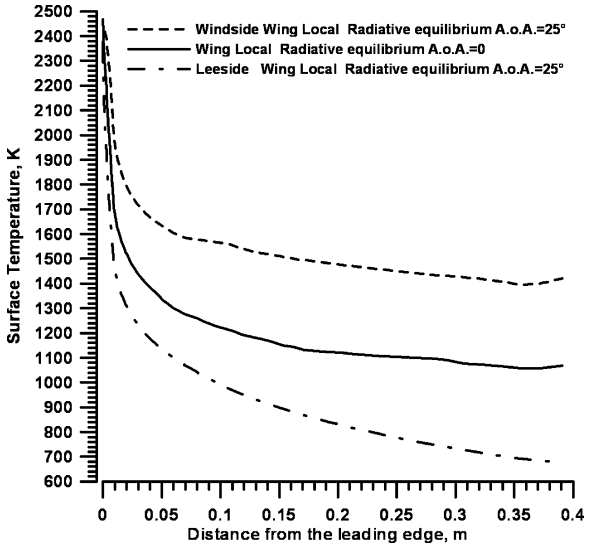

Fig. 3 Local radiative equilibrium temperature on two-dimensional body (wedge angle 12.5°) at 0 and 25-deg angle of attack, $M_\infty = 14.8$ and $Z = 60$ km.

zero angle of attack and for perfect gas

$$\delta_T/x \propto 1\Big/Pe_x^{\frac{1}{2}}, \qquad T_{\mathrm{wr}}^4 \propto (1/\sigma\varepsilon)[(T_r - T_{\mathrm{wr}})/\delta_T] \tag{7}$$

where x is the distance from stagnation point and Pe_x the local Peclet number ($Pe_x = Re_x Pr$). If $T_{\mathrm{wr}} \ll T_r$,

$$T_{\mathrm{wr}}^4 \propto 1/\sigma\varepsilon \left[\frac{Pe_L^{\frac{1}{2}}}{(x/L)^{\frac{1}{2}}}\right]\frac{T_r}{L} \tag{8}$$

where L is the length of the flat plate. Equation (8) shows that the fourth power of the radiative–adiabatic wall temperature (in laminar flow) 1) is inversely proportional to the characteristic boundary-layer thickness, 2) is proportional to the recovery temperature T_r, and 3) decreases with increasing distance from the nose tip as $x^{-1/2}$. Therefore, it is possible to estimate the distance x from the stagnation point at which the temperature is low enough to be bearable by a structural material; then it is possible to identify the needed UHTC tip insert length.

Two-dimensional geometries at angles of attack show a different $\dot{q}(x)$ distribution on the windside and on the leeside as shown in Fig. 3. The shape of the leading edge corresponds to the configurations shown in Fig. 4 and the flight conditions that will be introduced and discussed in Sec. IV. Figure 4 shows the main idea behind the BLTPS: Only the front part of the sharp body exceeds high temperature and needs UHTC materials; the rest of the body can be made of structural materials (hot structure). Needless to say, the expected mass of the BLTPS is dramatically less than the conventional systems (shuttlelike) because it is limited to the very front tips. Sharp bodies tend to behave as blunt bodies at high angles of attack by exposing more and more of the windside surface to high heat flux (as it is for the shuttle). The result of this observation is that the boundary-layer thermal protection (BLTP) concept does not apply if the angle of attack α exceeds some limits.

Figure 3 shows how a large angle of attack, for example, above 25 deg, implies that most of the windside structure is exposed to high heat fluxes, and consequently, it achieves high temperatures and would, therefore, survive only if one uses conventional thermal protection system (TPS). In conclusion, UHTC materials resist at very high temperature and may allow small radii of curvature and light protection systems. The only strong constraint, as will be discussed later, is to fly at a small angle of attack. Examination of Fig. 3 identifies two problems posed by the new concept of the TPS: 1) use of a material that can withstand stagnation point temperature and 2) a nose tip insert able to protect the rest of the structure without the need of tile- (or blanket-) type TPS.

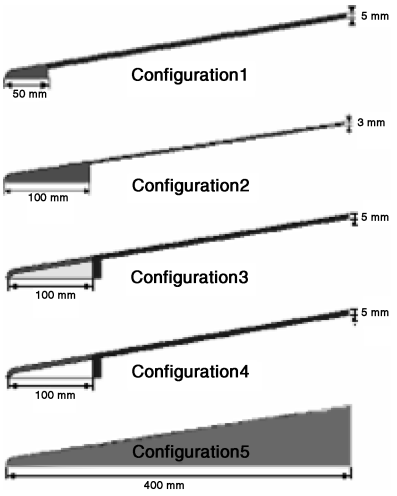

Fig. 4 Geometry and configurations of the sphere–cone: ▬, ZrB_2; ▭, SiC; ▬, inconel; and ▭, insulator ($\lambda = 0$).

III. Numerical Model

The Navier–Stokes equations for steady, laminar, hypersonic flow have been solved using a finite volume numerical code under the assumption of reacting gas in thermochemical nonequilibrium. The gas mixture has been considered as composed by five species, N_2, O_2, NO, N, and O (Ref. 8). A grid convergence analysis is made as described in the next paragraph. Nondissipative fluxes are calculated with Roe's method and dissipative fluxes with central schemes. For the (steady) simulations, pseudotime integration is performed using an explicit multistage Runge–Kutta scheme. Different wall boundary conditions have been considered. When the flowfield is uncoupled from the temperature distribution in the solid, that is, in the ideal case of a solid with zero thermal conductivity, the wall temperature boundary condition is specified as the radiation–equilibrium, according to the Stephan–Boltzmann relation,

$$\dot{q} = \left(-\lambda_s \frac{\partial T}{\partial n} - \rho \sum_i D_i h_i \frac{\partial c_i}{\partial n}\right)_w = \sigma\varepsilon T_{\mathrm{wr}}^4 \tag{9}$$

When the perfect gas model, or noncatalytic wall condition, is considered, the second term of the left-hand side of Eq. (9) vanishes.

For a reacting mixture, the chemical species boundary condition at the wall is prescribed. For a fully catalytic surfaces it is simply

$$c_i = (c_i)_{\mathrm{eq}} \tag{10}$$

where $(c_i)_{\mathrm{eq}}$ is the equilibrium composition at the local values of surface pressure and temperature.

For a noncatalytic wall, no species diffusions takes place at the wall, therefore,

$$\left(\frac{\partial c_i}{\partial n}\right)_w = 0 \tag{11}$$

When the aerothermodynamic field in the air is coupled with the local temperature field in the solid ($\lambda_s \neq 0$), the wall temperature is determined imposing the local balance between convective, conductive, and radiative heat fluxes,

$$\left(-\lambda \frac{\partial T}{\partial n} - \rho \sum_i D_i h_i \frac{\partial c_i}{\partial n}\right)_w = -\lambda_s \left(\frac{\partial T}{\partial n}\right)_{s,w} + \sigma\varepsilon T_w^4 \tag{12}$$

IV. Study Cases

A number of study cases has being selected to provide the evidence of the role played by 1) the extension of the UHTC insert at the leading-edge/nose tip, 2) the thermal conductivity of the UHTC materials, and 3) the angle of attack.

Table 1 Materials thermal properties[9]

Material	Density ρ, kg/m^3	Specific heat c_p, J/kg · K	Thermal conductivity λ_s, W/m · K
ZrB_2	6000	628	66
SiC	3210	660	60
Inconel-617	8456	456	15

All of the computations have been performed for sphere–cone and cylinder–wedge geometries. Both the cone and wedge curvature radius is 1 cm and the half-angle is 12.5 deg. These geometries simulate a sharp nose and the leading edge of a wing for the new vehicle concept. The radius of curvature of the cone has been chosen by a tradeoff between stagnation point temperature [a lower radius implies high stagnation temperature close to the limit of the TPS] and by the reduction of the drag of the vehicle and of its weight (large radius increases the wave drag and increases the TPS weight).

The internal configurations (Fig. 4) consist of different length massive noses (or leading edges) and different thickness walls. The total length is 40 cm. The chosen size of UHTC tip is driven by the weight, by the stagnation point temperature, and by the maximum temperature achievable by (at the end of the UHTC tip) the hot structure material.

Table 1 shows the physical properties of the materials under investigations at room temperature (ZrB_2, SiC, and Inconel-617). Materials thermal properties were assumed constant. Systematic computations did not show large differences if assuming temperature-dependent properties (according to Ref. 9).

New-generation materials for TPS are the UHTC, that is, a family of compounds that are chemically and physically stable at high temperatures, for example, above 2400°C, and in oxidizing atmospheres. These materials have melting temperatures above 3000°C, exhibit good thermal shock resistance, and can be modified with additives such as SiC to promote oxidation resistance.[10] In particular, ZrB_2–SiC and HfB_2–SiC are candidates for wing leading edges and nose tips where the highest temperatures are expected. These materials are also characterized by a relatively high thermal conductivity, which may prove to be beneficial for the stagnation point temperature.

Among the UHTC, ZrB_2 has been selected because of the lower density as compared to HfB_2 ($\rho_{ZrB_2} = 6000$ kg/m^3 and $\rho_{HfB_2} = 11{,}000$ kg/m^3). Other materials will be considered to improve weight, for instance, SiC/SiC. A constant value of emissivity of 0.8 has been assumed for ZrB_2. This value is justified by a number of experimental tests on a ZrB_2 sphere model heated by an arcjet and reaching a stagnation point temperature of about 2000°C. A two-color pyrometer measured an emissivity value ranging from 0.7 and 0.8. Oxidation of the ZrB_2 did not produce a large change in the emissivity.

The computations refer to the low-risk reentry trajectory shown in Fig. 1. The low-risk trajectory is characterized by a vehicle that is constrained for a part of the trajectory on a stagnation point heat flux constant curve.[1] In the case considered, the trajectory refers to a constant heat flux of 2.5 MW/m^2 (with a nose radius of 1 cm) from an altitude of 80–60 km. These extreme conditions have been chosen to better show the role of the investigated parameters. The selected point for the computations is $Z = 60$ km and $M_\infty = 14.8$; it has been chosen because at this altitude the continuum hypothesis is certainly verified and the computational fluid dynamics (CFD) results are more reliable.

For all of the cases considering the coupling between aerothermal field and thermal field of the solid, the simple assumption of perfect gas has been assumed to speed up the computation, justified by the fact that for a sharp leading edge and for the considered flight conditions the flow is almost chemically frozen in the shock layer.[11] (Also see Sec. IV.C.) Before the extensive computations performed in this work, a preliminary grid-convergence analysis has been carried out to find the best compromise between CPU time and accuracy. Numerical simulations for locally radiative equilibrium cases (grid in the solid body not considered) have been performed using meshes

Table 2 Computational grids

Grid	T_{sp}, K
40×30	2684
75×70	2710
100×90	2711

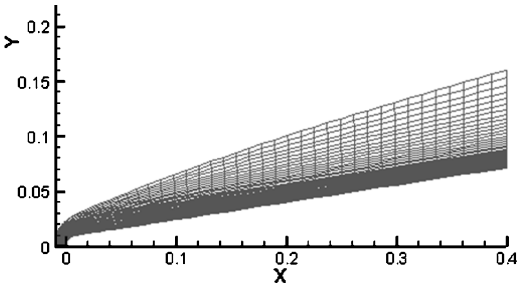

Fig. 5 Computational mesh, 75×70, where $\Delta n_{min} = 10^{-6}$.

with different grid points number, and the same minimum normal spacing to the body is 10^{-6} m. This parameter has been found by a number of previous numerical experiments to predict correctly the surface heating. Figure 5 shows the mesh with 75×70 grid points. The results obtained with the different grids reported in Table 2 show that the computed flowfields are already grid independent for the mesh with 75×70 grid points. Further increasing the number of grid points yields differences of the computed surface temperature (which is of the primary interest in this paper) at the stagnation point of less than 1%.

V. Results

A. Effect of Thermal Conductivity: Comparison Between Local and Global Radiative Equilibrium

At the selected orbital reentry conditions, convective heat transfer to the surface is partly conducted to the solid and partly reradiated into the atmosphere. When a steady state is achieved, global radiative equilibrium is established, in the sense that the (surface) overall convective heat flux is perfectly balanced by the overall surface radiative flux. When conduction in the solid may be neglected, that is, TPS materials with very low thermal conductivity, local equilibrium is established between radiative and convective heat transfer. The corresponding surface temperature will be referred to as local (for $\lambda_s = 0$) and global (for $\lambda_s \neq 0$) radiative equilibrium temperatures, respectively. TPS realized so far are characterized by refractory low-conductivity materials, acting as thermal insulators that cover and protect the metallic structure; the heat flux is alleviated making use of blunt configurations. The proposed new scenario for reentry vehicles introduces sharp geometries that are subjected to much higher heat fluxes and temperatures that conventional TPS materials would not sustain.

Figures 6 and 7 show the temperature distributions and contours for different axisymmetric configurations. In each case, the local radiative equilibrium temperature distributions are reported for comparison. The effect of high thermal conductivity of the UHTC is a strong decrease of the maximum tip temperature and an increase of the temperature downstream of the stagnation point, that is, the maximum temperature of the structural material, with respect to the local radiative equilibrium condition.

We note (Fig. 6) that with an increase in the bulk nose length from 50 to 100 mm (configurations 1 and 2) the stagnation point temperature decreases, as well as the structural materials interface temperature. If we assume that structural materials cannot stand temperature higher than 1500 K, then we must select configuration 2 (with 10 cm of UHTC insert). There are no substantial differences between configurations 3 and 4 (Fig. 7), corresponding to the same geometry and to the same external ZrB_2 shell but different materials for the nose insert.

The assumption of local radiative equilibrium (LRE) wall overestimates the stagnation point temperature and underestimates the surface temperature distribution downstream from the leading

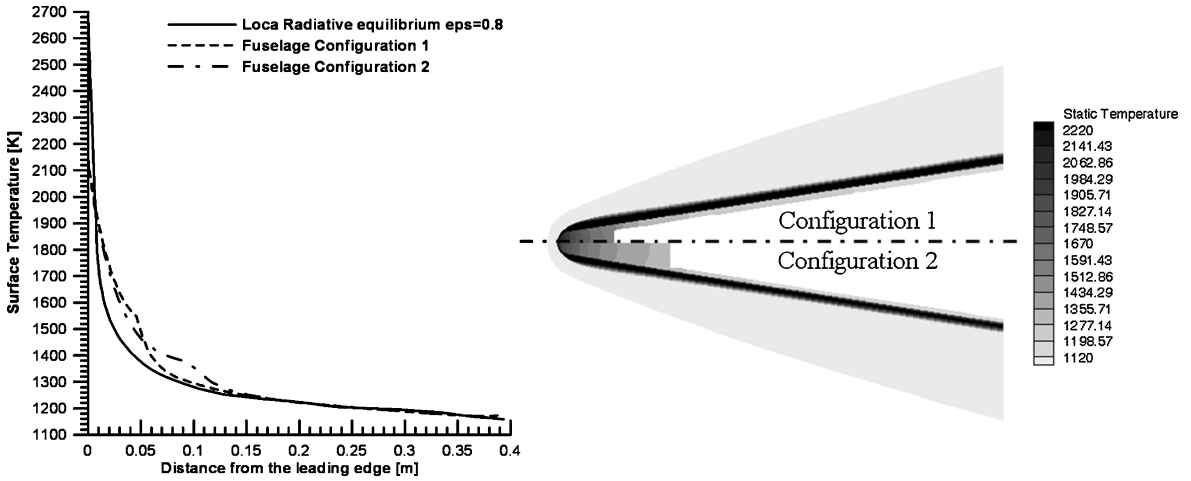

Fig. 6 Effect of ZrB_2 nose insert length: configurations 1 and 2 (axisymmetric).

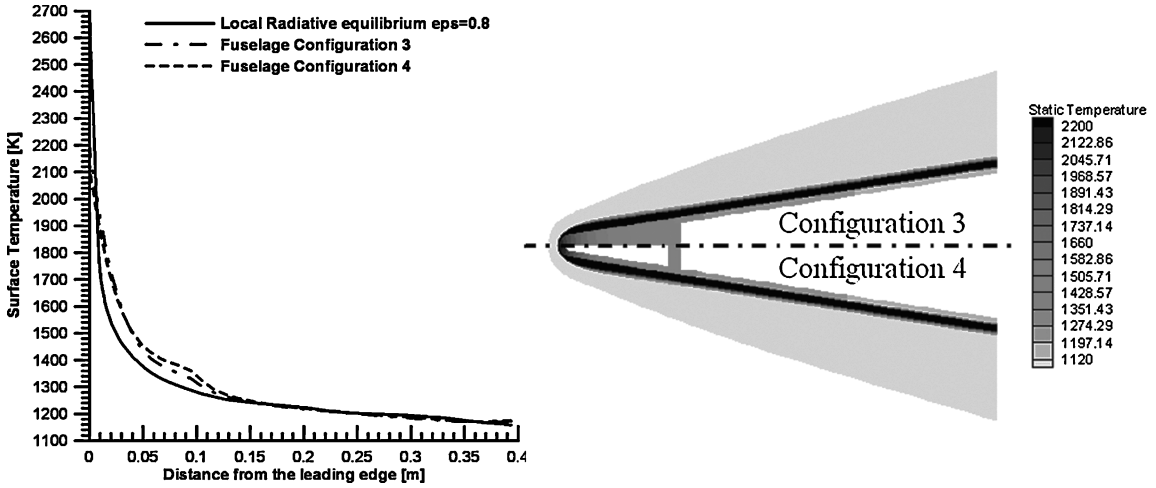

Fig. 7 Effect of SiC insert: configurations 3 and 4 (axisymmetric).

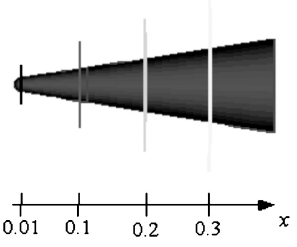

Fig. 8 Locations of the four stations.

edge. This effect is greater when TPS materials are characterized by high thermal conductivity.

B. Role of Angle of Attack

As mentioned in Sec. II, to ensure the efficiency of the BLTPS, new generation reentry vehicles need to fly at a low angle of attack to avoid exposing the windside metallic structure of the vehicle to high heat fluxes. On the other hand, during reentry, an appropriate angle of attack is necessary to ensure a sufficient C_L to sustain the vehicle. In other words, the BLTP benefit obtained at zero angle of attack must be checked at different angles of attack. To investigate this effect, a number of numerical simulations with different angles of attack have been performed. Polar plots have been prepared that show the value of the heat flux and of the surface temperature on different meridian planes (configuration 5) at four different locations (Fig. 8) on the fuselage.

Figure 9 shows the local convective heat fluxes at steady state, that is, global radiative equilibrium conditions, for an angle of attack of 15 deg and an axisymmetric configuration. On the windside, the convective heat flux is almost double that on the leeside. When flying at an angle of attack, the windside is exposed to higher heat fluxes than the leeside, and, therefore, heat will flow conductively across the fuselage between windside and leeside, leveling the temperatures and improving the thermal conditions of the TPS on the windside.

Figure 10 shows the skin-temperature distribution along the azimuth angle at the same locations considered in Fig. 7 at the global radiative equilibrium condition. Radial distance measures the skin temperature: larger circles are relative to stations near the stagnation point ($x = 0.01$, 0, 1 m), concentric circles (dashed) refer to zero angle of attack.

Figure 11 shows the local heat fluxes at steady state, that is, global radiative equilibrium conditions, for an angle of 15 deg and an axisymmetric configuration. The different profiles of surface heat flux (once the global radiation equilibrium has been reached) show that on the windside the convective heat flux is larger than the radiative one and vice versa on the leeside. The radial distance from the (black) inner circle measures the net heat flux entering the structure, that is, convective minus radiative. The inner circle corresponds to a perfect balance of the two fluxes (net heat flux equal to zero), that is, to LRE that would prevail if the thermal conductivity of the body skin is zero ($\lambda_s = 0$). The largest values correspond to stations close to the tip for which a large difference from the windside and leeside exists in heat flux and the relatively large thermal conductivity tends to level the temperatures at the sides (upper and lower) and at the front and back part. Both the axial and radial heat flux are responsible for the unbalance of the overall heat flux at each station.

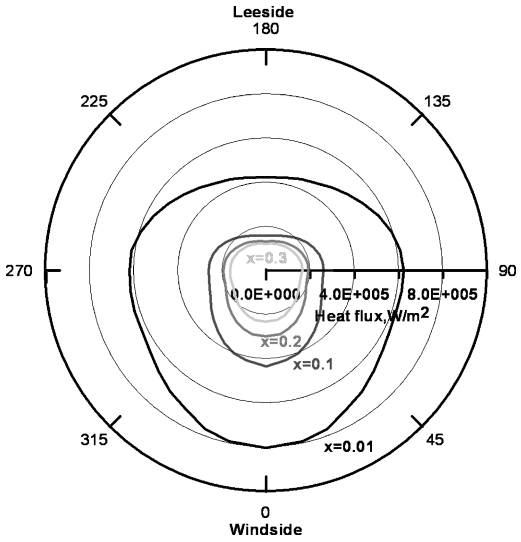

Fig. 9 Convective heat flux at different station along the body 15-deg angle of attack axisymmetric body.

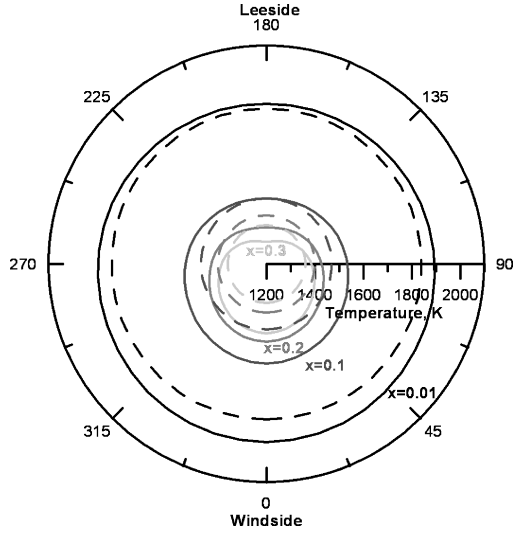

Fig. 10 Temperature at different stations along the body: – – –, 0 angle-of-attack and ——, 15-deg angle-of-attack axisymmetric body.

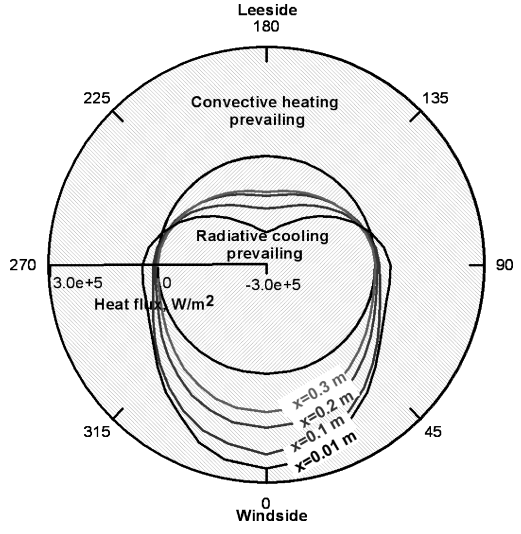

Fig. 11 Surface heat flux at different stations along nose–cone body at 15-deg angle of attack (axisymmetric body).

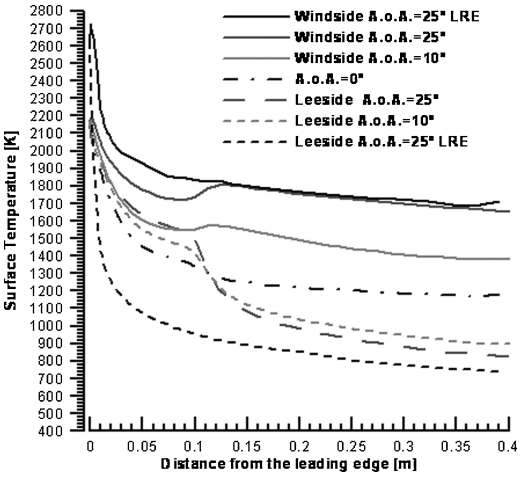

Fig. 12 Global radiative surface temperature for fuselage at different angles of attack, three-dimensional.

Figure 12 shows that the temperatures in the TPS zone do not change drastically up to 10 deg in three-dimensional (fuselage) cases with configuration 3. Increasing angle of attack up to 25 deg not only increases the temperature on the windside (as we would expect) but also on the leeside. These increases could be expected considering the high conductivity of TPS, which drives the heat from the hotter windside to the colder leeside until global radiative equilibrium is reached. For a sphere–cone geometry, at 10 cm downstream of the nose tip, and for an angle of attack larger than 10 deg, the temperature at the interface between the TPS and the structural material grows up to values that cannot be sustainable by any conventional structural material. This is explained by the heat flux from the ZrB_2 nose tip to the metallic structure across the interface and also by the lower thermal conductivity of the metallic structure that reduces the heat transfer from the hotter windside to the colder leeside.

State-of-the-art metallic structures cannot withstand, without TPS, temperatures higher than 1500 K (Ref. 12). Therefore, during reentry, for the considered configuration, the angle of attack cannot exceed 10 deg. This is another constraint for low-risk reentry trajectory for which it is necessary to monitor not only the stagnation point temperature but also the temperature of the structural material at the junction between the UHTC nose tip and the metallic structure.

Conditions can substantially improve on a half-cone with a bottom flat surface (typical of fuselage tips) because the belly exposure is reduced by an angle of 12.5 deg. We would then expect, roughly, a situation for the windside corresponding to an inclination of α minus 12.5 deg. The windside surface temperature at 25-deg angle of attack will, therefore, be close to that at 10 deg.

C. Role of Chemical Nonequilibrium and Surface Catalysis

All of the numerical simulations presented earlier have been performed considering a perfect gas model. For the parametric analyses this results in a considerable reduction of computer time, in particular when the thermal coupling between fluid and solid is taken into account. In general, during a reentry mission the real gas behavior must be considered because a large amount of kinetic energy of the hypersonic freestream is converted into thermal energy across the shock wave, hence, resulting in very high temperature near the nose and in the boundary layer where chemical reactions occur. When a sharp body is considered, the chemical reactions take place only in a thin shock layer that surrounds the sharp leading edge; therefore, only in this zone can we expect differences between catalytic and noncatalytic walls. Furthermore, the oblique shock wave corresponding to the slender nose is much weaker than the normal shock. When this thin shock layer and the high flow velocity are considered, the residence time between the shock and the body is smaller than the characteristic time necessary for the species to react chemically and to arrive at equilibrium.

To evidence the differences between the two models of ideal perfect gas and reacting mixture, numerical computations at the same

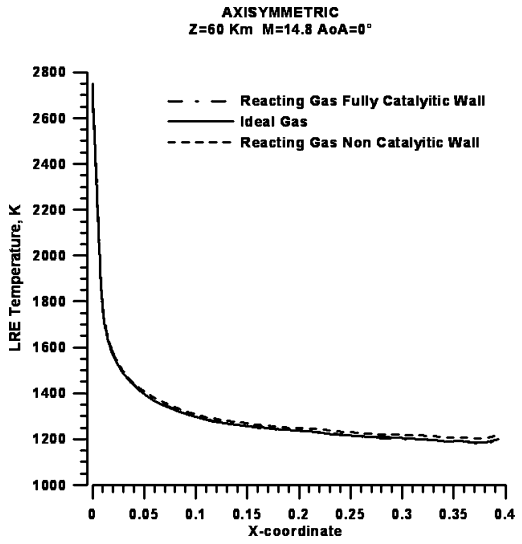

Fig. 13 Temperature distributions on axisymmetric body at zero angle of attack.

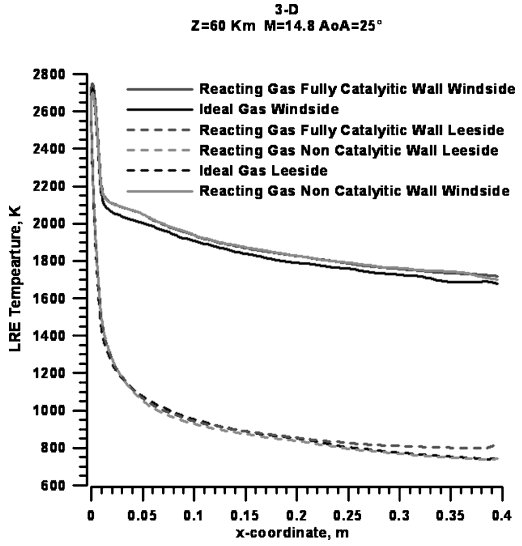

Fig. 14 Temperature distributions on axisymmetric body at 25-deg angle of attack.

flight condition, $M_\infty = 14.8$ and $Z = 60$ km, and with the LRE condition, $\lambda_s = 0$, have been carried out, considering an axisymmetric body at different angles of attack. The results of the simulations are summarized in Figs. 13 and 14. For the axisymmetric configuration, that is, fuselage nose tip, negligible differences can be seen between real gas and ideal gas, both at zero and at relatively high angles of attack. The differences between the case of a fully catalytic wall and noncatalytic wall are also very small, when compared to the case of blunt bodies, where peak values of the heat fluxes may vary by more than 100% at the same flow conditions.[11]

Similar results have been found at other positions along the trajectory. They all point out at the different importance of the catalytic effect in free flight for blunt (and high angle of attack) compared to sharp (and low angle of attack) bodies. In this last case, the gas almost does not dissociate for two reasons:

1) The weak oblique shock wave induces a temperature jump much smaller of that behind a normal shock wave (and therefore, no large dissociation is to be expected close to the wall).

2) The distance along the streamlines (from the entrance into the shock to the wall) is much larger for the blunt body so that the air has time to reach almost chemical equilibrium conditions (and large dissociations).

VI. Conclusions

The assumptions of nonthermally conducting materials, that is, the establishment of LRE may be misleading: The heat transfer inside the relatively high conductive UHTC material tends to lower the maximum tip temperature and to increase the temperature downstream from the stagnation point, that is, the maximum temperature of the structural material.

At relatively small angles of attack (less than or equal to 10 deg, for the study case analyzed) the temperature increase in the windside region downstream from the stagnation point remains within the limits of available advanced metallic structural materials.

When the angle of attack exceeds 10 deg, the temperature at the interface between TPS and the structural material may not be sustained by the structural material.

A tradeoff is needed because a high thermal conductivity of the UHTC is favorable for the tip but unfavorable for the structural materials. Parameters that must be checked are the length and weight of the tip: It should be longer (and heavier) to reduce the temperature of the structural material at the UHTC–metallic structure junction and, therefore, able to fly at larger angles of attack.

A flat bottom nose geometry with a two- or three-dimensional leading edge can be considered to reduce the aeroheating on the windside enabling a larger angle of attack.

A real gas seems, at first sight, to behave so differently from the ideal gas to jeopardize most of the conclusions reached assuming a constant composition air. In practice, the heat transfer over a sharp slender body does not differ much in the two cases due to the weak shock wave standoff distance at small angles of attack and to the very short time allowed to the air to dissociate. In conclusion, for the selected test cases, the air behaves almost as a frozen gas; this behavior has been confirmed by the results obtained in a recent paper[11] that compares the different effect of catalicity for blunt and sharp bodies in free flight and plasma wind tunnel conditions.

Acknowledgments

This work has been done with the partial support of Italian Aerospace Research Center and Italian Space Agency.

References

[1]Monti, R., and Pezzella, G., "A New Philosophy for the Design of Reentry Vehicles," *Space Technology*, Vol. 24, No. 4, 2004, pp. 179–191.

[2]Monti, R., Pezzella, G., Savino, R., Paterna, D., and Esposito, A., "Aerothermodynamic Study of an Advanced Thermal Protection System," *Proceedings of the 4th European Symposium on Hot Structure and Thermal Protection Systems for Space Vehicles*, ESA SP-521, Nov. 2002, pp. 139–146.

[3]Arnold, J., Johnson, S., and Wercinski, P., " SHARP: NASA's Research and Development Activities in Ultra High Temperature Ceramic Nose Caps and Leading Edges for Future Space Transportation Vehicles," Paper IAF-01-V5.02, IAF Symposium, Toulouse, France, Oct. 2001.

[4]Fahrenoltz, W. G., Hilmas, G. E., "NSF–AFOSR Joint Workshop on Future Ultra-High Temperature Materials," Final Rept., 2004, URL: web.umr.edu/∼uhtm [cited 11 Jan. 2005].

[5]Rasky, D. J., "Advanced Ceramic Matrix Composites for TPS," *Current Technology for Thermal Protection System*, NASA CP-3157, 1992, pp. 43–52.

[6]Arringhton, J. P., Jones, J. J., "Shuttle Performance: Lessons Learned," NASA CP-2283, Pt. 1, 1983, pp. 473–508.

[7]Tauber, M. E., "A Review of High Speed Convective, Heat-Transfer Computation Methods," NASA TP 2914, July 1989.

[8]Anderson, J. D., Jr., *Hypersonic and High Temperature Gas Dynamics*, Mc-Graw–Hill, New York, 1989, p. 498.

[9]"TPS-X Database," NASA Ames Research Center, http://tpsx.arc.nasa.gov [cited 15 Feb. 2005].

[10]Gasch, M., Ellerby, D., Irby, E., Beckman, S., Gusman, M., and Johnson, S., "Processing, Properties and Arc-Jet Oxidation of Hafnium Diboride/Silicon Carbide Ultra High Temperature Ceramics," *Journal of Materials Science*, Vol. 39, No. 19, 2004, pp. 5925–5937.

[11]Monti, R., Savino, R., and De Stefano Fumo, M., "On Wind Tunnel Testing of Low Risk Re-entry Trajectory," *4th International Symposium Atmospheric Reentry Vehicles and Systems*, 4th International Symposium Atmospheric Reentry Vehicles and Systems, AAAF, Arcachon, France, March 2005.

[12]"Dispersion-Strengthened High Temperature Materials, Material Properties and Application," PLANSEE, 2004, http:/www.plansee.com.